Upgrading the PtCu intermetallic compounds: The role of Pt and Cu in the alloy

R. Castillo, E. Dominguez Garcia, J.L. Santos, M.A. Centeno, F. Romero Sarria, Marco Daturi, J.A. Odriozola

Upgrading the PtCu intermetallic compounds: the role of Pt and Cu in the alloy

R. Castillo[a,b], E. Dominguez Garcia[b], J. L. Santos[a], M. A. Centeno[a], F. Romero Sarria[a], M. Daturi[b], J.A. Odriozola[a].*

[a] *Inorganic Chemistry department, University of Seville and Institute of Material Science of Seville (US-CSIC), 41092 Seville, Spain*

[b] *Normandie Univ, ENSICAEN, UNICAEN, CNRS, Laboratoire Catalyse et Spectrochimie, 14000 Caen, France*

**corresponding author: rcastillo4@us.es*

odrio@us.es

Abstract

This work is devoted to the study of the role of both metals in the intermetallic $Pt_xCu_y/\gamma Al_2O_3$ catalysts commonly employed in CO-PROX reaction. Therefore, monometallic Pt and Cu based catalysts and PtCu intermetallic compound with different molar ratios (Pt_3Cu_1 and Pt_1Cu_3) supported catalysts were carefully synthesized and deeply characterized. Room temperature CO adsorptions by FTIR spectroscopy were carried out on the mono- and intermetallic catalysts being the monometallic catalyst determinant for the study. From the analysis of the nature of the platinum surface in $Pt/\gamma Al_2O_3$, we have demonstrated that the role of Pt sites is based in the CO dissociation for the CO_2 formation and also how the platinum surface is partially blocked by leftovers from the synthesis. Moreover, the study of the $Cu/\gamma Al_2O_3$ and the bimetallic catalysts $Pt_xCu_y/\gamma Al_2O_3$ allowed elucidating the effect of the copper in the metallic site and support interphase as well as the role of copper in the hydrocarbon oxidation.

Keywords: Platinum, copper, alumina, CO adsorption, FTIR, CO-PROX**.**

1. Introduction

Recently, Pt-based intermetallic compounds (IMCs) have been studied such improved alternative for the monometallic catalysts for several catalytic processes[1]. Especially, the study of PtCu alloys is taking relevance in the energy-related catalytic processes [2–9]. In all of them, authors highlight that catalytic performance depends on surface structure and composition.

The better catalytic behavior of intermetallic Pt_xCu_y compounds respect to monometallic catalysts has been demonstrated in the preferential oxidation of CO [10]. This fact and the unknown active site nature of one of the most useful commercial catalyst for mobile devices [11] justify why several authors focus their work in the search of a suitable answer. Trying to clarify the role of both metals during the catalytic reaction, several studies have been reported about CO adsorption on Pt_xCu_y based catalysts, which are the object of this work. For instance, Komatsu et al. [1] showed the relationship of the metallic site electron density with the catalytic activity by the evaluation of the ν(CO) shift after the CO adsorptions on supported intermetallic compounds with different atomic ratio (Pt_3Cu_1 and Pt_1Cu_3).

However, before the study of the Pt_xCu_y intermetallic compounds, it is necessary to perform a complete characterization of the monometallic catalysts. CO adsorption on supported platinum catalysts has been studied by many authors due to the importance of these compounds in industry. Olsen and Masel [12] carried out the CO adsorption on Pt (111) single crystal finding two different carbonyl adsorption modes on platinum sites; a band related to linear carbonyls around 2080 cm^{-1} and another for two-fold bridge bound CO at 1850 cm^{-1}. A shift to higher wavenumber was observed depending on the CO coverage.

On the other hand, CO adsorption may provide information about metal coordination, geometry or adsorption mode on the active site. Jänsch et al. [13] studied the surface migration of adsorbed CO species on Pt (335) crystal by electronic excitation (electron stimulated migration). They distinguished two different adsorption modes: adsorbed CO on step sites and adsorbed CO on terrace sites, which their vibrational frequencies of CO stretch mode are clearly separated by around 25 cm^{-1}.

Platinum atoms with different particle size also could be located in different environments. Stakheev et al. [14] studied the electronic state and localization of supported Pt atoms by CO adsorption. Those authors observed three bands at 2000, 2060 and 2075 cm^{-1} and they concluded that the frequency shift was due to the CO adsorbed on platinum sites with a different environment. They explained how CO adsorption on more accessible platinum sites located near to the exposure surface involve different degrees of metal-support interaction or different particles shapes, and they related this kind of site with the band at 2075 cm^{-1}. The other two bands at 2060 and 2000 cm^{-1} were assigned to metallic sites with lower accessibility and also to CO adsorbed on high dispersed metallic platinum atoms.

In the cases of copper based catalyst, Cu^{n+}-CO surface carbonyls were located in a range from 2240 to 1916 cm^{-1}. Carbonyls formed by Cu^{+} ions are the most stable species of Cu^{n+}-CO complexes [15]. Dandekar et al. [16] identified them in a wide range from 2160 to 2080 cm^{-1} during the CO adsorption on supported Cu catalyst, assigning the carbonyl on Cu supported on γAl_2O_3 at around 2130 cm^{-1} . Conversely, Cu^{0}-CO complexes formed via a π bond with the copper atoms and carbonyls on Cu^{+2} ions are unstable at room temperature being detectable by CO adsorption only at low temperature (-196 ºC) [17].

Additionally, most of published results for PtCu based catalysts for CO-PROX reaction are based in a previous conditioning treatment under hydrogen environment in the range of 300 - 400ºC [1,18–21]. In this way, Romero-Sarria et al. [22] showed by *operando* FTIR study and CO adsorption on $PtCu/Al_2O_3$ catalyst, the effect of organic deposit (from the synthesis method) on the electron density of the active site and, therefore, its effect on the catalytic activity.

Although some authors argue that the organic molecules can be successfully removed without oxidative treatments, the presence of vibrational modes associated to the organic species in Raman and FTIR spectra of the catalysts surface after their conditioning process raises serious doubts on the effectiveness of their removing process [23].

In this work, we have studied the role of Pt and Cu in the active site of PtCu alloy supported on alumina using electron microscopy and probe molecules adsorption followed by FTIR spectroscopy. Especially, CO adsorption was carried out on $PtCu/\gamma Al_2O_3$ catalysts with different molar ratio (Pt_3Cu_1 and Pt_1Cu_3) as well as on supported Pt and Cu catalysts for the total understanding of the role of both metals in the alloy.

2. Experimental

2.1 Synthesis

Catalysts have been prepared in two steps. First, unsupported nanoparticles (NPs) were synthetized and then, NPs were supported on commercial γAl_2O_3 (10% wt) by a mechanical procedure.

PtCu intermetallic compound with different molar ratios (1:3 and 3:1) catalysts as well as Pt and Cu monometallic nanoparticles were synthesized following the

synthesis method reported by Taylor et al. [24]. Briefly, 25 ml of ethylene glycol (99%, PanReac) were heated at 110ºC in a bottom flask connected to a water condenser system for 1h. Then, the capping agent, which is poly(vinylpirrolidone) (PVP) (M_w = 55000), $H_2PtCl_6 \cdot xH_2O$ and $CuCl_2 \cdot 2H_2O$ (1:3:1 and 3:1:1 Cu:Pt:PVP molar ratio) were simultaneously added. For the monometallic catalysts, 1:1 metal:PVP molar ratio was employed. This solution was kept at 110ºC for 2 h. At this point, an excess of reducing agent is added dropwise and maintained under vigorous stirring for 15 min. The product was washed with acetone and dried at 60ºC. Finally, nanoparticles were supported on alumina.

2.2 Structural characterization

XRD patterns were acquired at room temperature in a X'Pert Pro PANalytical diffractometer using Cu Kα radiation source (40 mA, 45kV). Patterns were acquired in the range of $10° \leq 2\theta \leq 90°$ using a position sensitive detector with a step size of 0.05° and acquisition time of 300 s. Structural determination was performed by comparison with the database PDF2 ICDD2000 (Powder Diffraction File 2 International Centre for Diffraction Data, 2000).

High resolution transmission electron microscopy (HRTEM) was carried out using a FEI Talos electron microscope with a field emission source at an accelerating of 200 kV. Micrographs were taken with a side mounted Ceta 16M camera. Samples were deposited directly on 300 meshes holey carbon coated copper TEM-grid. XPS experiments were carried out at TEMPO beamline of SOLEIL Synchrotron (France). The conditioning of the catalysts were carried out at the own analysis chamber equipped with a SPECS Phoibos 150-NAP hemispherical electron analyzer under hydrogen flow atmosphere (20 mL/min). The pressure work during the conditioning treatment was 2 mbar. Spectra after the hydrogen treatment were taken in ultra-high vacuum conditions

at 5 x 10^{-9} mbar. Surface copper and platinum concentrations were estimated by the analysis of Pt 4*f* and Cu 3*p* photoelectrons. The incident energy was 300 eV which account for inelastic mean free paths (IMFP) of 5Å. Spectra were collected with pass energy of 20 eV. Shirley background was used and signal fitting was performed with Doniach-Sunjic for platinum photoelectrons and Gaussian/Lorentzian for copper photoelectrons.

2.3 Characterization by FTIR spectroscopy

Catalysts characterization by *in situ* FTIR spectroscopy was performed in a glass cell connected to a vacuum system, temperature controller and probe molecule system. O_2 and mainly CO as probe molecules were used in this work. The samples in a self-supported wafer form were introduced in the cell. Firstly, catalysts were conditioned under 6.5 mbar H_2 (99.97% Air Liquide) at 350ºC for 2h (heating rate of 10 C·min^{-1}). Then, temperature was cooled down until room temperature. H_2 environment was pumped at 200ºC to enhance the evacuation efficiency and for avoiding the organic rests deposition on the surface catalysts. Secondly, CO (99.99997%, Air Liquide) adsorption at room temperature was carried out when the vacuum in the cell got 10^{-6} mbar. CO probe molecule was added by aliquots of ~10^{-2} µmol until surface saturation. Similarly, O_2 (oxygen 5.0, Linde) addition experiment was carried out by the same method until saturation.

IR spectra were recorded by a Nicolet 6700 Fourier Transform IR spectrometer equipped by DTGS and MCT detectors. Spectra were collected using 128 scans with 4 cm^{-1} of resolution. Pellets were constituted by 15-20 mg of sample and 2 cm^2 of area. All spectra were normalized by weight (10 mg).

3. RESULTS AND DISCUSSION

3.1 Structural catalyst characterization

Alumina diffraction lines dominate over the diffraction peaks of the metallic phase making difficult the structural study of the nanoparticles. However, as described above, single-phase PtCu nanoparticles were first obtained, and afterwards supported on alumina allowing the structural analysis of the nanoparticles before supporting them. Figure 1 shows the XRD data of synthesized PtCu nanoparticles with different molar ratio (1:3 and 3:1) as well as the monometallic nanoparticles.

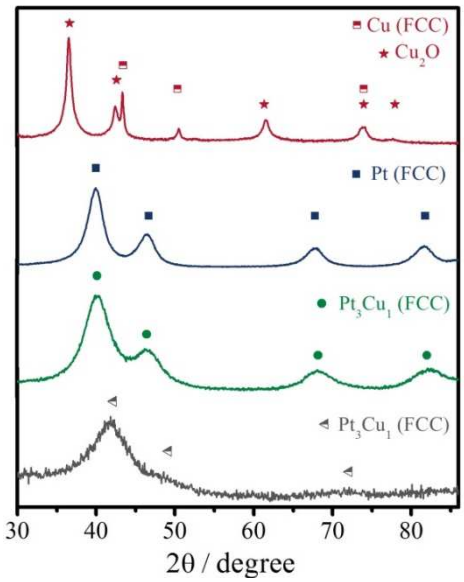

Figure 1. XRD data of prepared nanoparticles; Cu NPs (wine line), Pt NPs (blue line), Pt_3Cu_1 NPs (green line) and Pt_1Cu_3 NPs (yellow line)

PtCu bimetallic nanoparticles exhibit the typical diffractions patterns of well-defined PtCu bimetallic alloy nanoparticles with face centered cubic (FCC) structure and different molar ratio; Pt_3Cu_1 (JCDPS #00-048-1549) and Pt_1Cu_3 (JCDPS #00-035-1358), while platinum nanoparticles show diffraction lines corresponding to the metallic platinum phase with a FCC structure. The lattice parameters for both PtCu alloys were

estimated from the (111) PtCu diffraction. Assuming that PtCu alloys are solid solutions which follow the Vegard's Law, the real alloy compositions are shown in Table 1.

Table 1. Chemical composition and crystallite sizes (by XRD analysis) obtained for the synthesized unsupported nanoparticles.

	a (Å)	Composition	Size (nm)
Cu	3.6080	$(Cu_2O)_{70}@Cu_{30}$	20
Cu_2O	4.2520	$(Cu_2O)_{70}@Cu_{30}$	10.5
Pt	3.9100	-	3.8
Pt_3Cu_1	3.8691	$Pt_{74}Cu_{26}$	2.2
Pt_1Cu_3	3.7160	$Pt_{27}Cu_{73}$	1.5

In turn, XRD data of copper nanoparticles show a mixture of two phases: Cu_2O (JCDPS #00-001-1142) and metallic copper species (JCDPS #00-001-1241). The crystallite sizes of nanoparticles were estimated by Sherrer's equation. Since copper concentration increases in the alloy, particle size became smaller.

After the structural analysis, nanoparticles were supported on γAl_2O_3. Figure 2 shows a HRTEM image of Pt_1Cu_3 supported alumina nanoparticles. The average particle size is similar to the one calculated using XRD (~1,5 nm). As the observed average size of the supported nanoparticles obtained by HRTEM is similar, within the experimental error, to the ones estimated by XRD it may be concluded that nanoparticles were not affected by the supporting step.

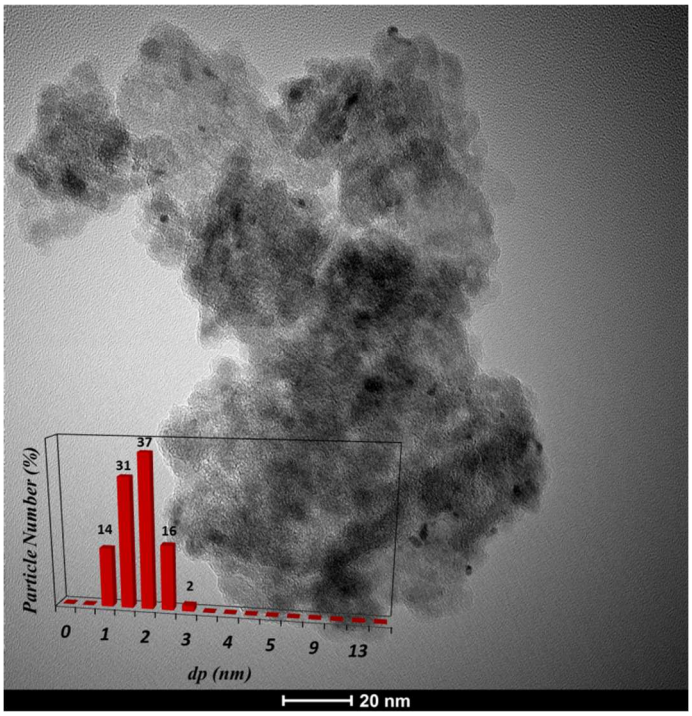

Figure 2. HRTEM image of $Pt_1Cu_3/\gamma Al_2O_3$ catalyst. The insert shows the size distribution of supported Pt_1Cu_3 nanoparticles.

Although, unsupported copper nanoparticles present an average size of 20 nm, according to the Sherrer's method, once supported on alumina these copper nanoparticles were not detected by HRTEM. Nevertheless, STEM analysis in mapping mode (Figure 3) revealed a high homogeneous distribution of copper onto the alumina support. This account for a very small average diameter of the copper nanoparticles and points to the difficulty of estimating average sizes by XRD particularly when overlapping diffraction lines are present. Probably, the size of the nanoparticles is close to the detection limit of the TEM microscope in the bright field imaging mode being the analyzed crystallite size by XRD the one corresponding to Cu_2O species.

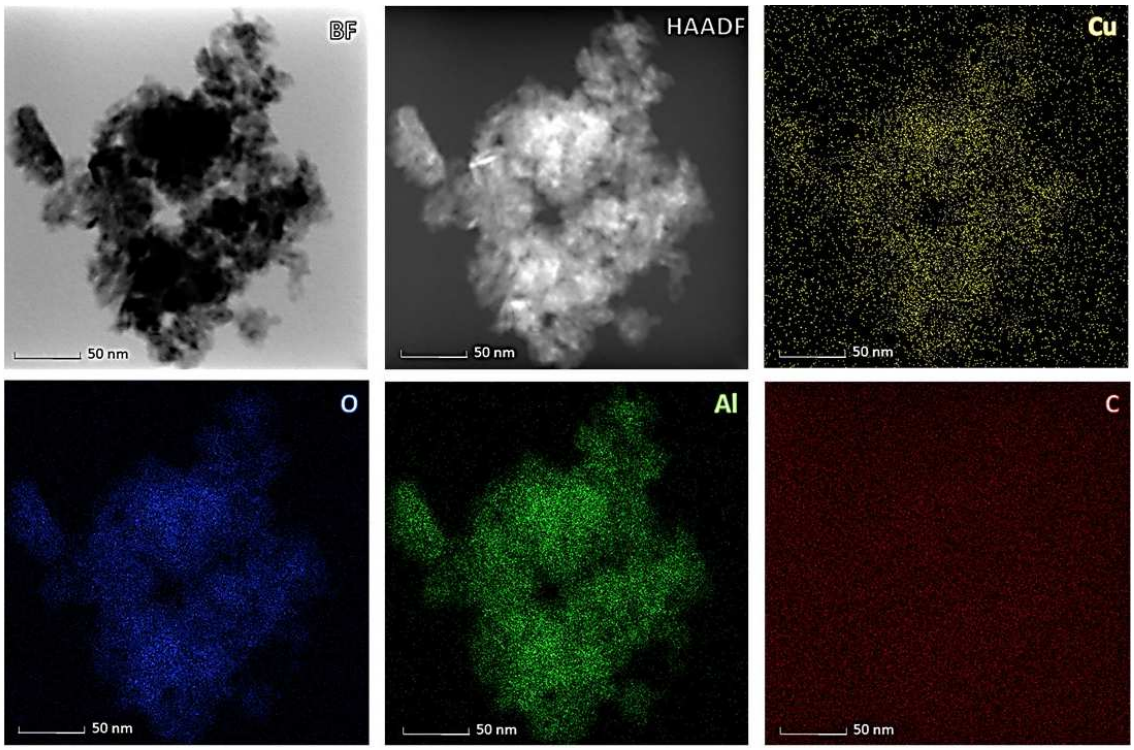

Figure 3. STEM images of Cu/γAl_2O_3 catalyst; bright-field (BF), High-angle annular dark-field (HAADF) and EDX elemental mapping of Cu, O, Al and C.

3.2 CO adsorption on Pt/γAl_2O_3 catalyst

Figure 4 shows the IR spectra upon successive CO adsorption experiments on previously H_2-reduced Pt/γAl_2O_3 catalyst. Carbon monoxide was progressively introduced in the FTIR system after the conditioning treatment at 350ºC for 2 hours under hydrogen atmosphere. Spectra showed in figure 4.a present a shift of the absorbed carbonyls species on the platinum surface from the initial band at 2055 cm^{-1} to a predominant band at 2065 cm^{-1} assigned to CO adsorbed on metallic platinum species [15,25]. This band shows a shoulder at 2010 cm^{-1} assigned by Bazin et al. [26] to adsorbed CO on small platinum nanoparticles (average particle sizes below 1.5 nm) (Figure 4.b). Also, those authors assigned the observed band at 1943 cm^{-1} to bridged CO species adsorbed at the metal-support interface. However, this later assignment remains uncertain since the different nature of the support.

The weak band observed at 2130 cm^{-1} can be related with the possible presence of absorbed CO on $Pt^{\delta+}$ atoms present at platinum nanoparticles/alumina interface. Finally, bridged CO adsorption species were not found in the region between 1800 cm^{-1} and 1850 cm^{-1} (Figure 4.a), in the form of a broad and weak feature.

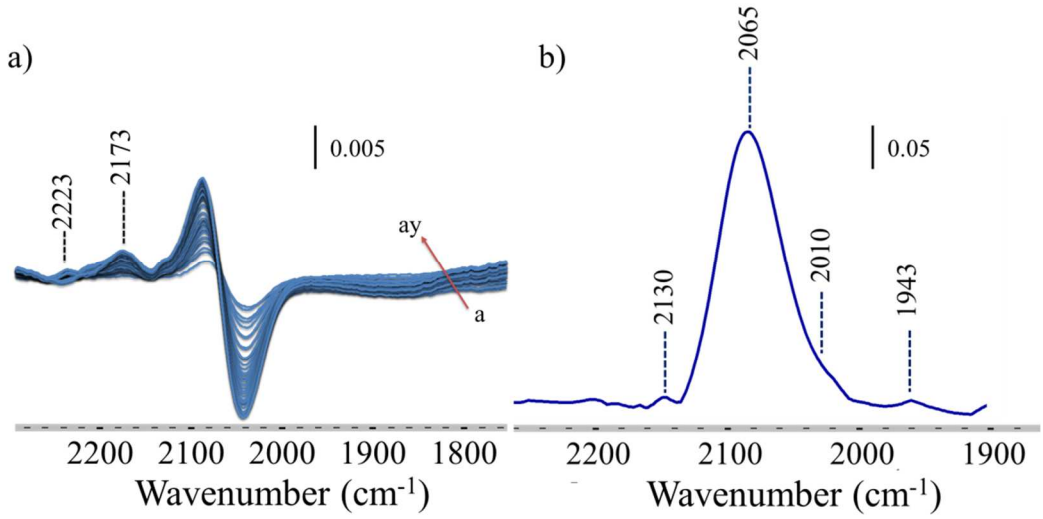

Figure 4. **a)** Difference FTIR spectra during CO adsorption on Pt/γAl_2O_3 from (a) 0.1 µmol CO to (ay) 13 µmol CO. An isosbestic point due to the species transformation is observed. Difference spectra displayed, obtained by subtracting the corresponding spectra acquired before gas exposure. **b)** FTIR spectra recorded after CO adsorption on Pt/γAl_2O_3.

Moreover, bands at 2173 cm^{-1} and 2223 cm^{-1} assigned to CO absorbed on alumina surface were observed in the subtracted spectra. The characterization of Lewis and Bronsted acid sites by CO adsorption on the γAl_2O_3 surface has been extensively reported by many authors [27–30]. Physisorbed CO results in a band at 2140 cm^{-1}, whereas CO interacting with surface OH groups gives rise to a band at 2155 cm^{-1}, while another massif from 2180 cm^{-1} to 2245 cm^{-1} accounts for CO interacting with Lewis acid sites. Therefore, the bands at 2173 cm^{-1} and 2223 cm^{-1} are assigned to CO adsorbed on Al^{3+} cations in octahedral, $(Al^{+3}\text{-}CO)_{oct}$, and tetrahedral, $(Al^{+3}\text{-}CO)_{tet}$, coordination, respectively [31].

An additional set of bands in the 1000-1800 cm^{-1} regions associated to the presence of residual carbonaceous species adsorbed on the support surface are also observed (Figure 5a). Weak bands at 1494 and 1420 cm^{-1} are ascribed to C-H bending modes in CH_3 ($\delta(CH_3)_{as}$) and CH_2 ($\delta(CH_2)$) [32]. The ascription of the bands at 1684, 1577, 1460, 1378 and 1290 cm^{-1} is controversial. Borodko et al. [33] claims that the bands at 1680, 1450 and 1370 cm^{-1} correspond to C-H deformation modes of amide carbonyls from residual PVP decomposition products, while Romero-Sarria et al. [22] assigned bands around 1577 and 1460 cm^{-1} to acetate species, and bands around 1370 cm^{-1} to the presence of different hydrocarbons on the alumina surface. However, Finocchio et al. [32,34] assign the band at 1684 cm^{-1} and the weak shoulder around 1640 cm^{-1} to C=C stretching (ν(C=C)), and the bands at 1577, 1460, 1378 and 1290 cm^{-1} to OCO stretching modes of carboxylate species and CH deformations. In this way, Busca et al. [35] observed the presence of the same set of bands during the oxidation of propane and propene on Co_3O_4 and $MgCrO_4$. These authors related the aforementioned set of bands to the presence of acrylate species that are intermediates in the oxidation of hydrocarbons on the alumina surface (Figure 5b).

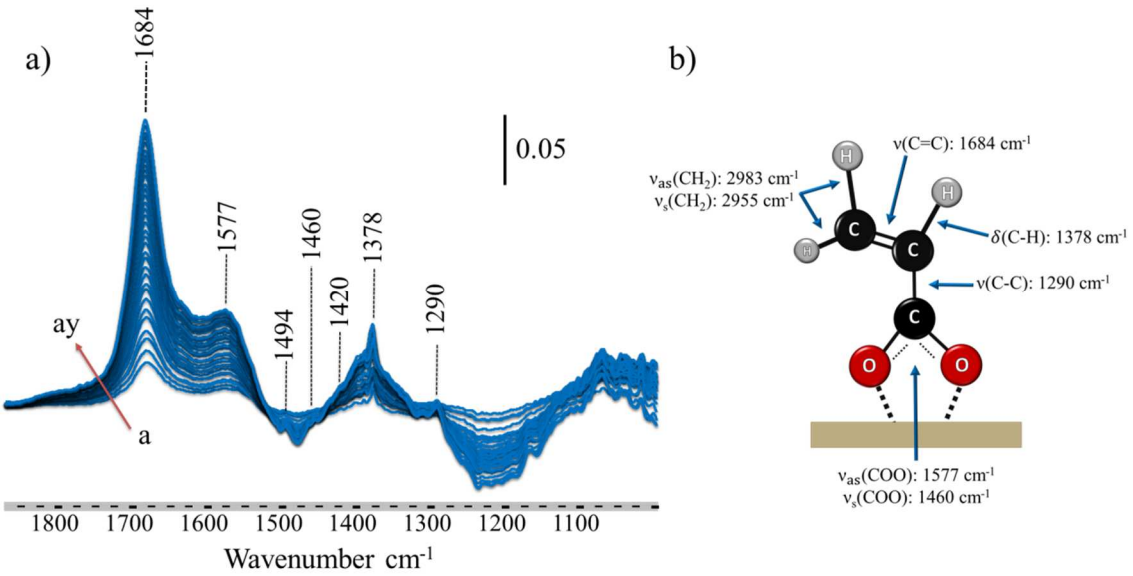

Figure 5. Acquired FTIR spectra during the CO adsorption on Pt/γAl_2O_3 from (a) 0.1 µmol CO to (ay) 13 µmol CO. **a)** Evolution of the region between 1000 cm^{-1} and 1800 cm^{-1}. **b)** Observed vibrational modes in the acrylates species formation.

Moreover, the presence of bands corresponding to C-H vibrational modes in the 2800-3100 cm^{-1} region (not shown), confirms the previous assignments. Bands at 2924 cm^{-1} and 2838 cm^{-1} were assigned to the symmetric ($\nu(CH_3)_s$ and asymmetric $\nu(CH_3)_{as}$) C-H stretching modes, respectively [36]. Busca et al. [37] explained the origin of the found bands during the formaldehyde adsorption and transformation on different oxide surfaces. They related the band at 2960 cm^{-1} to δCH vibrational modes, which can be shifted by Fermi resonance effects. Finally, bands around 2955 and 2983 cm^{-1} would correspond to $\nu(CH_2)_s$ and $\nu(CH_2)_{as}$ stretching modes.

Modification of the vibrational features of surface OH in the 3800–3500 cm^{-1} region (not shown) during CO adsorption on Pt/γAl_2O_3 were not observed since bands overlap as a result of the presence of adsorbed water.

This spectroscopic evidence points out the complex situation of the surface, presenting a large number of residual species from synthesis, as well as transformation products of those residuals upon reducing treatments.

The interaction of CO with the catalyst surface at RT allows the evaluation of the efficiency of the employed conditioning treatment. Analysis of the gas phase upon CO adsorption allows observing the production of CO_2. On increasing the number of CO doses, an oscillation of the bands intensity of CO_2 gas phase (around 2348 cm^{-1}) was observed. Figure 6 shows the CO_2 band area evolution during the CO adsorption after the conditioning treatment. It shows a small CO_2 production during the first doses of CO adsorption after H_2 treatment. The CO_2 production decreases when the added CO amount increases, being zero at CO saturation coverages. The number of edge and kink surface sites as well as the relative occurrence of (100) and (111) faces has been estimated assuming cubo-octahedron particle shape and the model developed by Van Hardeveld and Hartog [38]. The total amount of CO_2 species evolved is estimated in orders of magnitude below the number of edge and kink sites and (100) surface sites of 1.5 nm cubo-octahedron particles, respectively.

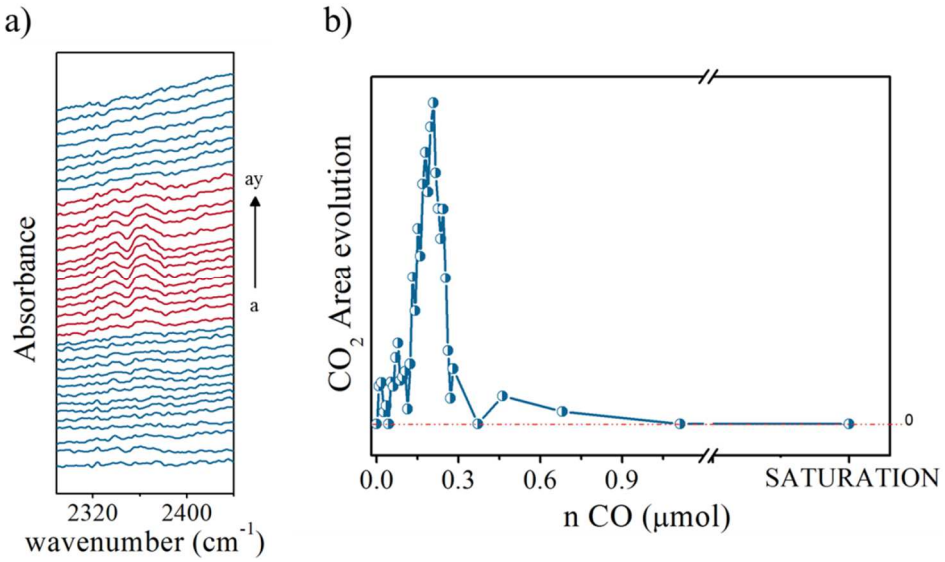

Figure 6. Evolution of the CO_2 gas phase area bands during the CO adsorption on Pt/γAl_2O_3 after H_2 treatment. **a)** FTIR spectra region from 2290 to 2440 cm^{-1}. **b)** CO_2 gas phase band intensity evolution as a function of the added CO doses. Note that the time between doses is always the same and the CO amount added is also the same in each dose (0,009 μmol CO/dose).

As the CO_2 production is well below the number of step and kink sites that are the most reactive ones the presence of surface carbon overlayers from the synthesis step after H_2 treatment is suggested. Thus, these carbon deposits block nanoparticle active sites being the Pt surface only partially available for CO adsorption. Adsorbed CO may dissociate on platinum nanoparticles forming adsorbed oxygen and additional deposits of carbon on the nanoparticles surface [39,40]. The increment of the CO_2 concentration in the atmosphere might be due to the reaction between the CO and the so-formed oxygen for producing CO_2 gas (Eq. (1)). McCrea et al. [40] showed different pathway for the CO_2 formation by CO dissociation on Pt crystal surfaces, as well as for the ignition of CO (Eq. (4)), CO oxidation via a Langmuir-Hinshelwood kinetics mechanism (Eq. (5)) or surface carbon oxidation by an ignition process (Eq. (6)), but most of them consider the presence of molecular oxygen for the oxidation process. These authors state that CO dissociation, more favorable on the (100) surface than in the

(111) one, occurs just at temperatures above ~225ºC. On the other hand, Minot [41] demonstrate the influence of CO pressure on the formation of CO_2 (Eq(7)) through the formation of Pt-CO-CO multilayers leaving behind adsorbed carbon species but again high temperatures are required for the reaction. The very low CO conversion into CO_2 accounting for less than 0,1% of the most reactive surface sites is in accordance with the high temperature requirements for any of these reactions, while at the same time suggests a large blocking of Pt surface sites by the presence of carbon.

(1) $CO\,(g) + \frac{1}{2}\,O_2\,(g) \rightarrow CO_2\,(g)$

(2) $CO\,(g) + * \rightarrow CO*$

(3) $CO* \rightarrow C* + O*$

(4) $CO\,(g) + O* \rightarrow CO_2\,(g) + *$

(5) $CO* + O* \rightarrow CO_2\,(g) + * + *$

(6) $C* + 2O* \rightarrow CO_2\,(g) + * + * + *$

(7) $CO_2\,(g) + C* \leftrightarrow 2CO\,(g) + *$

3.2.1 O_2 introduction on Pt/γAl_2O_3 catalyst

The ignition of residual carbon deposits was analyzed by introducing O_2 doses in the IR cell. Successive oxygen doses were submitted to the non-conditioned (fresh catalyst) or H_2-treated Pt/γAl_2O_3 catalyst to evaluate the presence of surface carbon deposits. The goal of this experiment was to estimate the amount of surface carbon deposits in the conditioned catalyst and the effects of adsorbed oxygen from the CO dissociation on the platinum oxidation state. First, the evolution of the CO_2 bands was followed during the oxygen small doses introduction (Figure 7a). CO_2 production increases on increasing the amount of added oxygen being higher the amount of CO_2 for the fresh catalyst,

which may indicate that the H_2 treatment results in a decrease of surface carbon. In addition to gas phase CO_2, adsorbed CO species appear, Figure 7.b. The spectra in the CO stretching region show bands at 2064, 2130 and 2174 cm^{-1} assigned to linearly adsorbed CO on metallic platinum nanoparticles, CO adsorbed on platinum atoms with low electron density ($Pt^{\delta+}$ atoms) and absorbed CO on $(Al^{+3})_{Oct}$, respectively. The spectrum of the adsorbed CO phase is irrespective of the treatment but the intensity for the H_2-treated sample is lower indicating that carbon deposits are partially removed with this treatment and that the Pt oxidation state is not modified by adding O_2 doses at room temperature. The presence of adsorbed CO has been observed upon O_2 adsorption on carbon covered Pt surfaces while adsorbed oxygen is not detected when the adsorption is carried out on clean surfaces [40]. Therefore, the presence of carbon deposits that may be partially removed upon H_2 reduction treatment is stated.

In both case, for the non-conditioned catalyst and after H_2 treatment, there is a remarkable surface carbon amount that can be removed by O_2 adsorption at RT. The total amount of gas phase CO_2 observed upon introduction of 1 µmol O_2 in the IR cell is ~$7{,}0 \cdot 10^{14}$ and ~$2{,}5 \cdot 10^{14}$ molecules for the fresh and the H_2-treated catalysts, respectively. However, the reaction conditions during the oxygen addition (exposure time, temperature, oxygen amount, etc.) are not enough for the total removal of surface carbon through a gasification process, so CO_2 bands are present for all the experiment.

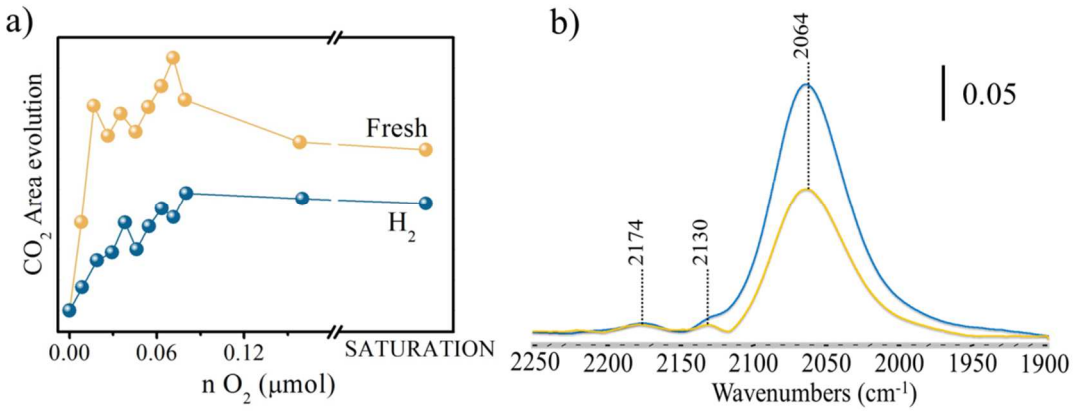

Figure 7. a) Evolution of the CO_2 band area during the small doses oxygen addiction on non-activated $Pt/\gamma Al_2O_3$ (yellow color) and on $Pt/\gamma Al_2O_3$ after H_2 treatment (blue color). **b)** Absorbed CO after oxygen addiction on non-activated $Pt/\gamma Al_2O_3$ (yellow color) and on $Pt/\gamma Al_2O_3$ pretreated under H_2 atmosphere (blue color).

3.3 CO adsorption on $Cu/\gamma Al_2O_3$ catalyst

FTIR difference spectra recorded during CO adsorption on $Cu/\gamma Al_2O_3$ after H_2 treatment are plotted in Figure 8. Together with the presence of adsorbed CO species, Figure 8.b, there is a clear modification of the OH stretching region. In Figure 8.a spectra of the OH stretching region during CO adsorption after H_2 treatment are plotted showing bands at 3622, 3650, 3684 and 3755 cm^{-1} ascribed to OH stretching modes of newly formed bi- and mono-dentate hydrogen carbonates [42], OH groups linked to tetrahedral and octahedral Al^{+3} cations [43] or alternatively bridged on pentacoordinated aluminum centers [29] and terminal OH groups on surface tetrahedral aluminum sites [44] or alternatively on octahedral aluminum centers [29], respectively. It is clearly seen that CO adsorption induces a perturbation on the hydroxyls coordinated with the tetrahedral aluminum sites, demonstrating that one of the carbonyl features interacts more with the support than with the copper species. Quantitatively, lower intensity of the bands assigned to the OH vibrational modes was observed after H_2 treatment, being the intensity of the bands witnessing for the coordination of CO on different sites (from 1950 to 2200 cm^{-1}) affected in the same way, coherently. The similar behavior of both

groups of bands is related with the strength of the support-metal interaction, i.e. copper-alumina interaction is stronger after H_2 treatment.

According to Bechoux et al. [43] conclusions that studied CO adsorptions on Ag/Al_2O_3 after reducing and oxidizing pretreatments, copper atoms interact with the closer OH groups (neighboring basic oxygen) decreasing the available copper sites for the CO adsorption. Also, neighbor basic oxygen atoms transfer electron density to the copper atoms allowing the formation of Cu^+-CO complexes and their characteristic band at 2122 cm^{-1}. Additionally to the expected metallic site of copper nanoparticles after reduction, the presence of Cu^+ species could be related to the electrophilic behavior of copper atoms in the presence of CO molecules proposed by Komatsu et al. [1] that concluded that Cu atoms adsorb available oxygen atoms from CO dissociation originating $Cu^{\delta+}$ species.

Interestingly, a main band can be observed at 2123 cm^{-1} with a shoulder to lower wavenumber at 2098 cm^{-1} (Figure 8b). In addition, a weak band at 2165 cm^{-1} can be observed. Different possibilities could be proposed for the nature of such Cu sites. K.I. Hadjiivanov and G.N. Vayssilvov [15] described frequencies of the surface carbonyls absorbed on the copper atoms as a function of the copper oxidation state, concluding that the characteristic band of linear carbonyls adsorbed on Cu^{2+} (Cu^{2+}-CO) is located between 2220 and 2150 cm^{-1}, band of carbonyls adsorbed on Cu^+ (Cu^+-CO) is located between 2160 and 2080 cm^{-1}, while carbonyls adsorbed on metallic copper (Cu^0-CO) show a weak band lower than 2130 cm^{-1}.

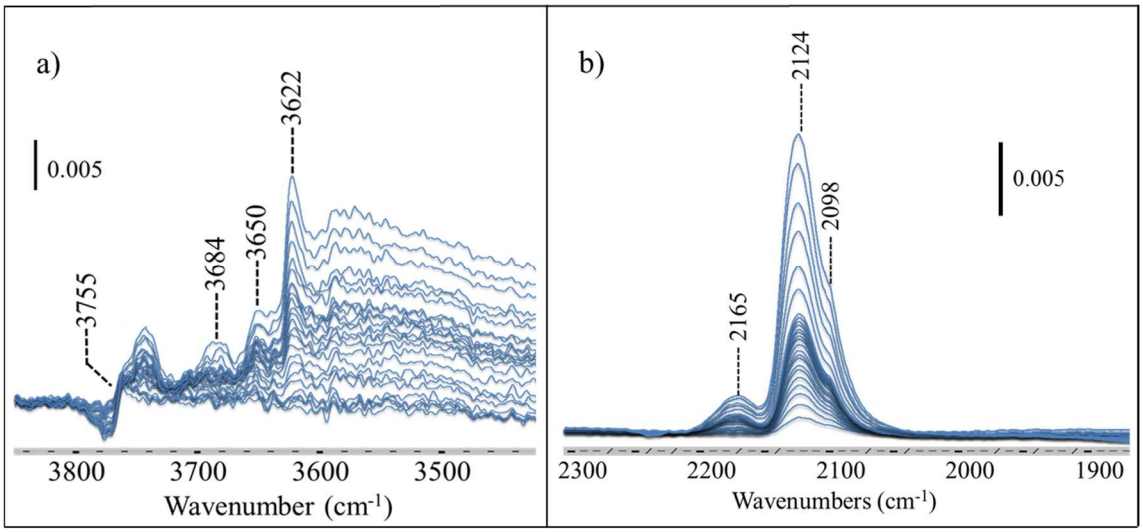

Figure 8. Difference FTIR spectra during the CO adsorption on Cu/γAl_2O_3 after H_2 treatment from (a) 0.1 µmol CO to (ay) 20 µmol CO: **(a)** ν(OH) vibrational modes of the OH groups **(b)** CO adsorbed on copper sites.

On the other hand, Zecchina et al. [45] carried out a CO adsorption on silica supported copper catalyst after progressive reduction steps under H_2 environment at different temperatures. When Cu/SiO_2 was reduced at 400ºC, they observed two bands; a weak band at 2163 cm^{-1} and a sharper band at 2136 cm^{-1}. They concluded that both bands are due to CO adsorbed on small Cu^+ atoms on extended faces and edges and steps respectively. Also, Hadjiivanov et al. [15] proposed the band at 2165 cm^{-1} due to carbonyls absorbed on Cu^{2+} species. Moreover, when the reduction temperature was increased during the CO adsorption on Cu/SiO_2, a new shoulder around 2100 cm^{-1} was observed and they assigned this band to CO adsorbed on metallic copper or CO adsorbed on a Cu-rich non stoichiometric Cu_2O phase. Thus, the CO adsorption on Cu^{2+} species, carbonyls adsorbed on small particles of Cu^+ (probably located in the metal-support interface) and CO absorption on metallic copper could be assigned to the found band at 2165, 2122 and 2098 cm^{-1}, respectively, in agreement with Zecchina et al. [45] and Hadjiivanov's [15] conclusions. However, the presence of Cu^{2+} species is unlikely after the reducing H_2 treatment. It means that band at 2165 cm^{-1} could be due to

carbonyls adsorbed on Cu^{+} species or CO absorbed on the Al^{3+} cations in octahedral coordination ($(Al^{+3}\text{-}CO)_{oct}$) on the alumina support. Note that tetrahedral sites on alumina are blocked by copper particles avoiding the CO adsorption. Thus, the assignment of bands at 2122 cm^{-1} to Cu^{+} species after a reducing treatment could be explained with support-metal interactions upon –OH groups evacuation.

In summary, observed bands at 2098, 2122 and 2163 cm^{-1} after both treatments are related with the CO adsorption on metallic copper species, CO adsorbed on Cu^{+} species and adsorbed CO on Al^{3+} cations with octahedral coordination ($(Al^{+3}\text{-}CO)_{oct}$), more than on Cu^{2+} sites, unexpected here. Moreover, an important detail is the absence of CO_2 bands during the CO adsorption on $Cu/\gamma Al_2O_3$.

As expected, the CO adsorption at room temperature after H_2 treatment on $Cu/\gamma Al_2O_3$ exhibits also several bands in the region between 1100 and 1800 cm^{-1}. First, during the CO adsorption after H_2 treatment, bands at 1229, 1264, 1374, 1396, 1432, 1468, 1579, 1619 and 1657 cm^{-1} were observed (Figure 9).

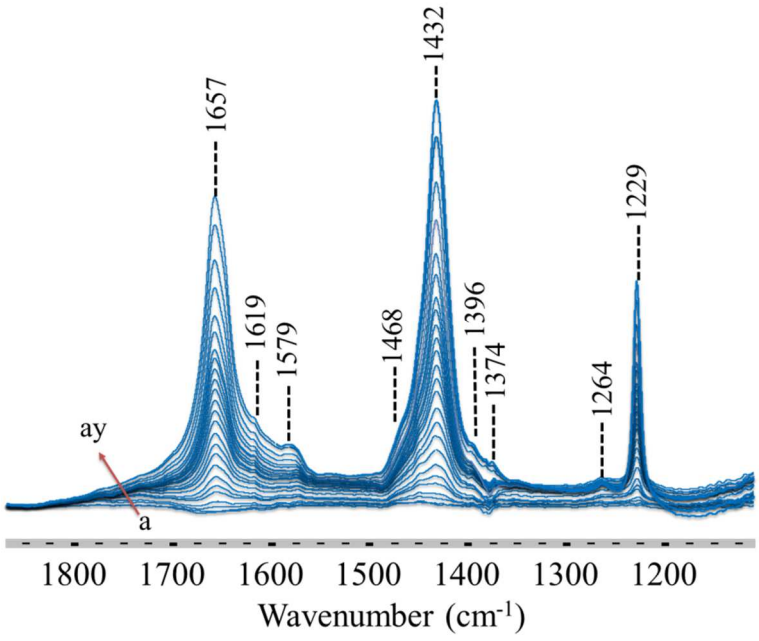

Figure 9. FTIR spectra during CO adsorption on Cu/γAl_2O_3 after H_2 treatment from (a) 0.1 μmol CO to (ay) 20 μmol CO.

Strong carbonate bands were observed during the CO adsorption on Cu/γAl_2O_3 after H_2 treatment at 1657, 1432 and 1229 cm^{-1}. Their assignment is not simple due to the different structures showed by carbonates. The main observed bands correspond to hydrogen-carbonates species; ν_{as}(COO) at 1657 cm^{-1}, ν_s(COO) at 1432 cm^{-1} and δ(OH) at 1229 cm^{-1}. However, different carbonates species on the surface of alumina should be expected and may be present as traces. Weak bands at 1579, 1468 and 1264 cm^{-1} correspond to υ_{as}(COO), υ_s(COO) and υ(C-C) vibrational modes of adsorbed acetates species, while bands at 1374, 1396 and 1579 cm^{-1} characteristic of formate species were found [46]. However, the intensity of the latter is extremely weak, even not showing the CH stretching vibrational mode. Thus, only hydrogen-carbonates species were considered for the surface analysis.

Föttinger et al. [47] studied the possible pathways mechanism of carbonate formations on Pd/Al_2O_3 upon CO adsorption, and they concluded that it takes place via "Water Gas Shift" reaction between CO and alumina hydroxyl groups followed by the reaction of the formed CO_2 with other OH groups.

Also, bands around 1620, 1579 and 1264 cm^{-1} are increasing and they could be related with the ν(C=O), $\nu(COO)_{as}$ and $\nu(COO)_s$ vibrational modes characteristic of bidentate or bridged carbonates species formation, due to the interaction of the formed CO_2 with basic oxygen atoms, probably from the oxidized copper species [48].

3.4 CO adsorption on PtCu/γAl$_2$O$_3$ catalysts

After having characterized the materials with single metal particles, we can now address the bimetallic catalysts. For the total understanding of the Pt$_x$Cu$_y$ alloy behavior and the role of both metals, CO adsorption on Pt$_3$Cu$_1$/γAl$_2$O$_3$ was carried out after H$_2$ pretreatments.

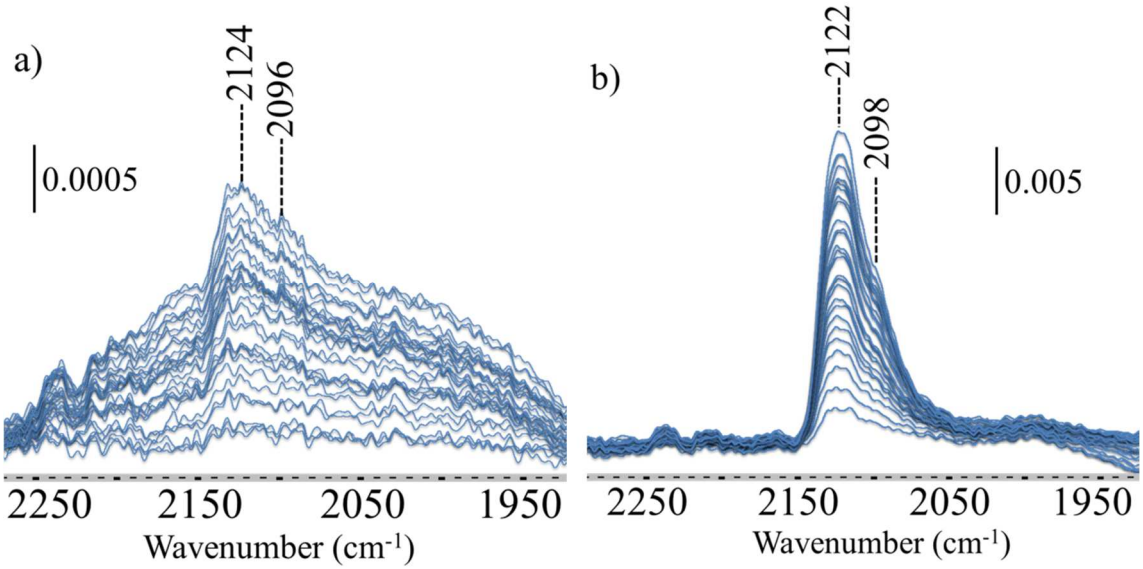

Figure 10. Difference FTIR spectra during CO adsorption at room temperature on: **(a)** Pt$_3$Cu$_1$/γAl$_2$O$_3$ and **(b)** Pt$_1$Cu$_3$/γAl$_2$O$_3$.

Figure 10a shows the acquired spectra during the CO adsorption on Pt$_3$Cu$_1$/γ*A*l$_2$O$_3$ after the conditioning treatment. The Pt$_3$Cu$_1$ sample showed weak bands at 2096 and 2124 cm^{-1}. CO adsorption on Pt/γAl$_2$O$_3$ (Figure 4) showed a main band at 2065 cm^{-1}, with a shoulder at 2010 cm^{-1} characteristic of metallic platinum species with different particle sizes, while CO adsorption on Cu/γAl$_2$O$_3$ showed two bands at 2098 and 2122 cm^{-1} (Figure 8.b).

Surface analysis of unsupported Pt$_3$Cu$_1$ nanoparticles carried out by APXPS (Figure 11) with inelastic mean free path of 5Å reveals a surface composition of the

nanoparticles of 57% Cu and 33% Pt, i.e. there is a high surface copper enrichment after the conditioning treatment. Therefore, the Cu-rich surface leads us to assign the bands at 2096 and 2124 cm^{-1} during the CO adsorption on $Pt_3Cu_1/\gamma Al_2O_3$ after H_2 treatment to Cu^+ and metallic copper species (Figure 10a). The low intensity of the carbonyl bands impeaches the observation of the bands related to platinum sites.

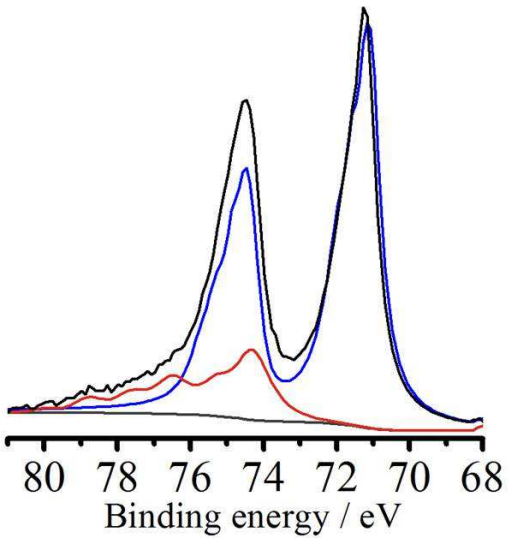

Figure 11. Pt 4*f* and Cu 3*p* APXP spectrum of unsupported Pt_3Cu_1 nanoparticles. Blue line corresponds to platinum component and red line to the copper one.

During the CO adsorption on $Pt_1Cu_3/\gamma Al_2O_3$ (Figure 10b), bands characteristic of adsorbed carbonyls on copper species appear at the same frequency, 2098 and 2122 cm^{-1}, as observed on the monometallic samples. Considering the Cu-rich surface composition between 63 and 83% of copper species calculated by APXPS of the unsupported Pt_1Cu_3 nanoparticles (spectrum not shown), the surface of $Pt_1Cu_3/\gamma Al_2O_3$ catalyst is extremtly similar to the $Cu/\gamma Al_2O_3$ surface and the observed bands at 2098 and 2122 cm^{-1} could be related to carbonyls adsorbed on metallic copper species and Cu^+ species respectivily. The different intensities are due to the greater interaction of copper atoms in the $Pt_3Cu_1/\gamma Al_2O_3$ catalyst with the alumina OH groups, which

supposes less available sites for the CO adsorption. Finally, the band at 2172 cm^{-1} was assigned to carbonyls adsorbed to Al^{+3} cations in octahedral coordination ($(Al^{+3}\text{-}CO)_{oct}$).

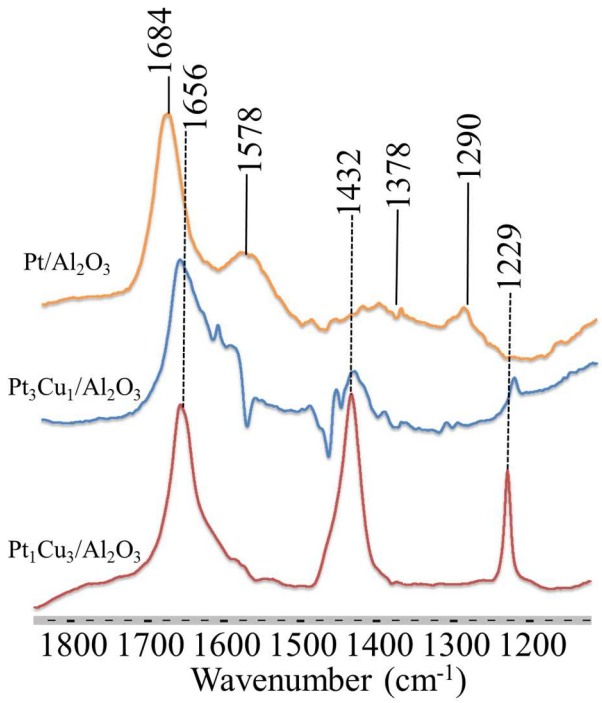

Figure 12. Difference FTIR spectra of CO adsorption at room temperature on $Pt/\gamma Al_2O_3$ after H_2 treatment (orange color), CO adsorption on $Pt_3Cu_1/\gamma Al_2O_3$ (blue color) and CO adsorption on $Pt_1Cu_3/\gamma Al_2O_3$ (red color). Bands pointed with solid lines correspond to species on $Pt/\gamma Al_2O_3$ and bands pointed with dashed lines correspond to species on $Pt_xCu_y/\gamma Al_2O_3$ catalysts.

Figure 12 shows a comparison of the carbonates spectral region between FTIR spectra of CO adsorption on $Pt/\gamma Al_2O_3$ after H_2 treatment and CO adsorption on the $Pt_3Cu_1/\gamma Al_2O_3$ and $Pt_1Cu_3/\gamma Al_2O_3$ catalysts.

After the CO adsorption on $Pt/\gamma Al_2O_3$ pretreated under hydrogen treatments, bands at 1684, 1578, 1378 and 1290 cm^{-1} assigned to acrylates species were observed (Figure 4). However, the addition of small amounts of copper produces different surfaces species. After the CO adsorption on $Pt_1Cu_3/\gamma Al_2O_3$ pretreated under H_2 atmosphere, remarkable bands at 1656, 1432 and 1229 cm^{-1} assigned to hydrogen-carbonates were observed. However, after the CO adsorption on $Pt_3Cu_1/\gamma Al_2O_3$, the

decrement of bands at 1578 and 1460 cm^{-1} characteristic of absorbed acetates species is showed. Thus, copper species in PtCu alloy (3:1 molar ratio) promotes the surface hydrocarbons oxidation. Initial acrylates species formed by platinum atoms are oxidized to acetate species [49,50]. With the increment of the oxidation degree, acetate species are oxidized to CO_2 and H_2O, which leads to an increase of the sites availability. Finally, CO_2 and H_2O form hydrogen-carbonates (Figure 13).

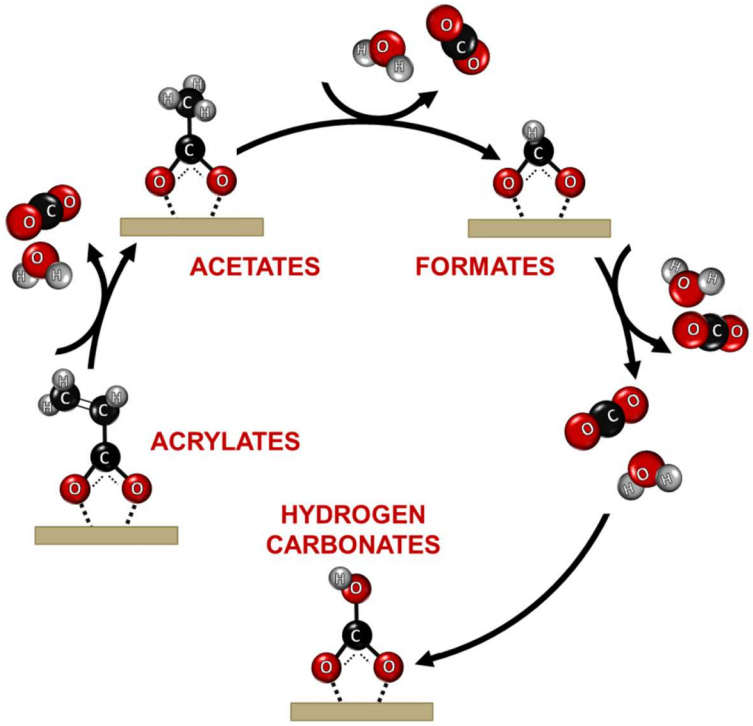

Figure 13. Schematic mechanism for the hydrocarbon oxidation on the $Pt_1Cu_3/\gamma Al_2O_3$ surface.

The appearance of the decreasing bands of acetate species in samples pretreated under hydrogen environment means a lower reaction rate for the hydrocarbons oxidation. Small CO_2 production was observed during the CO adsorption on $Pt_3Cu_1/\gamma Al_2O_3$ after H_2 treatment. On the other hand, after the CO adsorption on $Pt_1Cu_3/\gamma Al_2O_3$ catalyst, only the final product is appreciable.

Therefore, according to the above comparison, $Pt_1Cu_3/\gamma Al_2O_3$ catalysts shows a low reaction rate for the surface hydrocarbons oxydation respect to the PtCu alloy 3:1 molar ratio. The acetate species oxidation to CO_2, clearly evidenced with the decrement of bands at 1470 and 1580 cm^{-1}, and the absence of CO_2 transformation into hydrogen-carbonates could explain the higher CO conversion and selectivity to CO_2 for the intermetallic PtCu 1:3 molar ratio catalyst during the preferential oxidation of CO [22,51].

Conclusions

The role of both metals in the intermetallic compound PtCu was studied by CO adsorption. PtCu nanoparticles alloy with different molar ratio supported on alumina as well as the monometallic solids were synthesized and characterized. The monometal platinum catalysts characterization revealed the role of platinum atoms on the CO dissociation to form CO_2 by different pathways, evidencing a remarkable effect of the organic residuals from the synthesis step. The influence of the metal-support interaction on the active sites was evaluated by the correlations between the alumina OH groups and carbonyls absorbed on the active site of supported copper nanoparticles. Moreover, the effect of copper on hydrocarbons oxidation was highlighted considering the different reaction properties.

Acknowledgements

Financial support for this work has been obtained from the Spanish Ministerio de Economía y Competitividad (MINECO) (ENE2013-47880-C3-2-R) co-financed by FEDER funds from the European Union. Authors acknowledge to SOLEIL synchrotron for provision of beamtime for carrying out the APXPS experiments.

References

[1] T. Komatsu, M. Takasaki, K. Ozawa, S. Furukawa, A. Muramatsu, J. Phys. Chem. C. 117 (2013) 10483–10491.

[2] J. Tang, L. Deng, S. Xiao, H. Deng, X. Zhang, W. Hu, J. Phys. Chem. C. 119 (2015) 21515–21527.

[3] J. Knudsen, A.U. Nilekar, R.T. Vang, J. Schnadt, E.L. Kunkes, J.A. Dumesic, M. Mavrikakis, F. Besenbacher, J. Am. Chem. Soc. 129 (2007) 6485–6490.

[4] S. Zhou, B. Varughese, B. Eichhorn, G. Jackson, K. McIlwrath, Angew. Chemie - Int. Ed. 44 (2005) 4539–4543.

[5] I.E.L. Stephens, A.S. Bondarenko, U. Grønbjerg, J. Rossmeisl, I. Chorkendorff, Energy Environ. Sci. 5 (2012) 6744–6762.

[6] B. Geboes, J. Ustarroz, K. Sentosun, H. Vanrompay, A. Hubin, S. Bals, T. Breugelmans, ACS Catal. 6 (2016) 5856–5864.

[7] C.J. Zhang, R.J. Baxter, P. Hu, A. Alavi, M.H. Lee, J. Chem. Phys. 115 (2001) 5272–5277.

[8] D. Xu, Z. Liu, H. Yang, Q. Liu, J. Zhang, J. Fang, S. Zou, K. Sun, Angew. Chemie - Int. Ed. 48 (2009) 4217–4221.

[9] D. Xu, S. Bliznakov, Z. Liu, J. Fang, N. Dimitrov, Angew. Chemie - Int. Ed. 49 (2010) 1282–1285.

[10] K. Liu, A. Wang, T. Zhang, ACS Catal. 2 (2012) 1165–1178.

[11] L. Shore, W. F.Ruettinger, R.J. Farrauto, Platinum group metal promoted copper oxidation catalysts and methods for carbon monoxide remediation., US 6,913,739 B2, 2005.

[12] C.W. Olsen, R.I. Masel, Surf. Sci. 201 (1988) 444–460.

[13] J.H. J., J. Xu, J.T. Yates, J. Chem. Phys. 99 (1993) 721–724.

[14] A.Y. Stakheev, E.S. Shpiro, N.I. Jaeger, G. Schulz-EKloff, Catal. Letters. 32 (1995) 147–158.

[15] K.I. Hadjiivanov, G.N. Vayssilov, Adv. Catal. 47 (2002) 307–511.

[16] A. Dandekar, M.A. Vannice, J. Catal. 178 (1998) 621–639.

[17] J.M.G. Amores, V.S. Escribano, G. Busca, V. Lorenzelli, J. Mater. Chem. 4 (1994) 965–971.

[18] T.R. Reina, S. Ivanova, O.H. Laguna, M.A. Centeno, J.A. Odriozola, Appl. Catal. B Environ. 197 (2016) 67–72.

[19] O.H. Laguna, E.M. Ngassa, S. Oraá, A. Álvarez, M.I. Domínguez, F. Romero-Sarria, G. Arzamendi, L.M. Gandía, M.A. Centeno, J.A. Odriozola, Catal. Today. 180 (2012) 105–110.

[20] G. Avgouropoulos, T. Ioannides, C. Papadopoulou, Catal. Today. 75 (2002) 157–167.

[21] A. Manasilp, E. Gulari, Appl. Catal. B Environ. 37 (2002) 17–25.

[22] F. Romero-Sarria, S. Garcia-Dali, S. Palma, E.M. Jimenez-Barrera, L. Oliviero, P. Bazin, J.A. Odriozola, Surf. Sci. 648 (2015) 84–91.

[23] M. Luo, Y. Hong, W. Yao, C. Huang, Q. Xu, Q. Wu, J. Mater. Chem. A. 3 (2015) 2770–2775.

[24] E. Taylor, S. Chen, J. Tao, L. Wu, Y. Zhu, J. Chen, ChemSusChem. 6 (2013) 1863–1867.

[25] P. Hollins, Surf. Sci. Rep. 16 (1992) 51–94.

[26] P. Bazin, O. Saur, J.C. Lavalley, M. Daturi, G. Blanchard, Phys. Chem. Chem. Phys. 7 (2005) 187–194.

[27] F. Maugé, J. Lavalley, J. Catal. 137 (1992) 69–76.

[28] C. Morterra, V. Bolis, G. Magnacca, Faraday Discuss. 92 (1996) 1991–1999.

[29] M. Digne, P. Sautet, P. Raybaud, P. Euzen, H. Toulhoat, J. Catal. 211 (2002) 1–5.

[30] M. Digne, P. Sautet, P. Raybaud, P. Euzen, H. Toulhoat, J. Catal. 226 (2004) 54–

68.

[31] M. Haneda, E. Joubert, J. Ménézo, D. Duprez, J. Barbier, N. Bion, M. Daturi, J. Saussey, J. Lavalley, H. Hamada, Phys. Chem. Chem. Phys. 3 (2001) 1366–1370.

[32] E. Finocchio, G. Busca, V. Lorenzelli, F. Ingegneria, P. Kennedy, R.J. Willey, J. Chem. Soc. Faraday Trans. 90 (1994) 3347–3356.

[33] Y. Borodko, H. Sook Lee, S. Hoon Joo, Y. Zhang, G. Somorjai, J. Phys. Chem. C. 114 (2010) 1117–1126.

[34] E. Finocchio, G. Busca, V. Lorenzelli, V.S. Escribanob, J. Chem. Soc. Faraday Trans. 1. 92 (1996) 1587–1593.

[35] G. Busca, M. Daturi, E. Finocchio, V. Lorenzelli, G. Ramis, R.J. Willey, Catal. Today. 33 (1997) 239–249.

[36] E. Finocchio, M. Daturi, C. Binet, J.C. Lavalley, G. Blanchard, Catal. Today. 52 (1999) 53–63.

[37] G. Busca, J. Lamotte, J. Lavalley, V. Lorenzelli, J. Am. Chem. Soc. 106 (1987) 5197–5202.

[38] R.V.A.N. Hardeveld, F. Hartog, Surf. Sci. 15 (1969) 189–230.

[39] M. Rinnemo, D. Kulginov, S. Johansson, K.L. Wong, V.P. Zhdanov, B. Kasemo, Surf. Sci. 376 (1997) 297–309.

[40] K.R. Mccrea, J.S. Parker, G.A. Somorjai, J. Phys. Chem. B. 106 (2002) 10854–10863.

[41] C. Minot, Catal. Today. 89 (2004) 357–362.

[42] E. Köck, M. Kogler, T. Bielz, B. Klötzer, S. Penner, J. Phys. Chem. C. 117 (2013) 17666–17673.

[43] K. Bechoux, O. Marie, M. Daturi, G. Delahay, C. Petitto, S. Rousseau, G. Blanchard, Catal. Today. 197 (2012) 155–161.

[44] C. Morterra, G. Ghiotti, F. Boccuzzi, S. Coluccia, J. Catal. 51 (1978) 299–313.

[45] A. Zecchina, G. Spoto, D. Scarano, J. Electron Spectros. Relat. Phenomena. 45 (1987) 269–279.

[46] A. Davydov, Molecular Spectroscopy of Oxide Catalyst Surfaces, 2003.

[47] K. Föttinger, R. Schlögl, G. Rupprechter, Chem. Commun. 3 (2008) 320–322.

[48] K.I. Hadjiivanov, G.N. Vayssilov, Adv. Catal. 47 (2002) 307–511.

[49] A.A. Davydov, V.G. Mikhaltchenko, V.D. Sokolovskii, G.K. Boreskov, J. Catal. 55 (1978) 299–313.

[50] A.M. Gabelnick, A.T. Capitano, S.M. Kane, J.L. Gland, D.A. Fischer, J. Am. Chem. Soc. 122 (2000) 143–149.

[51] K. Liu, A. Wang, T. Zhang, ACS Catal. 2 (2012) 1165–1178.

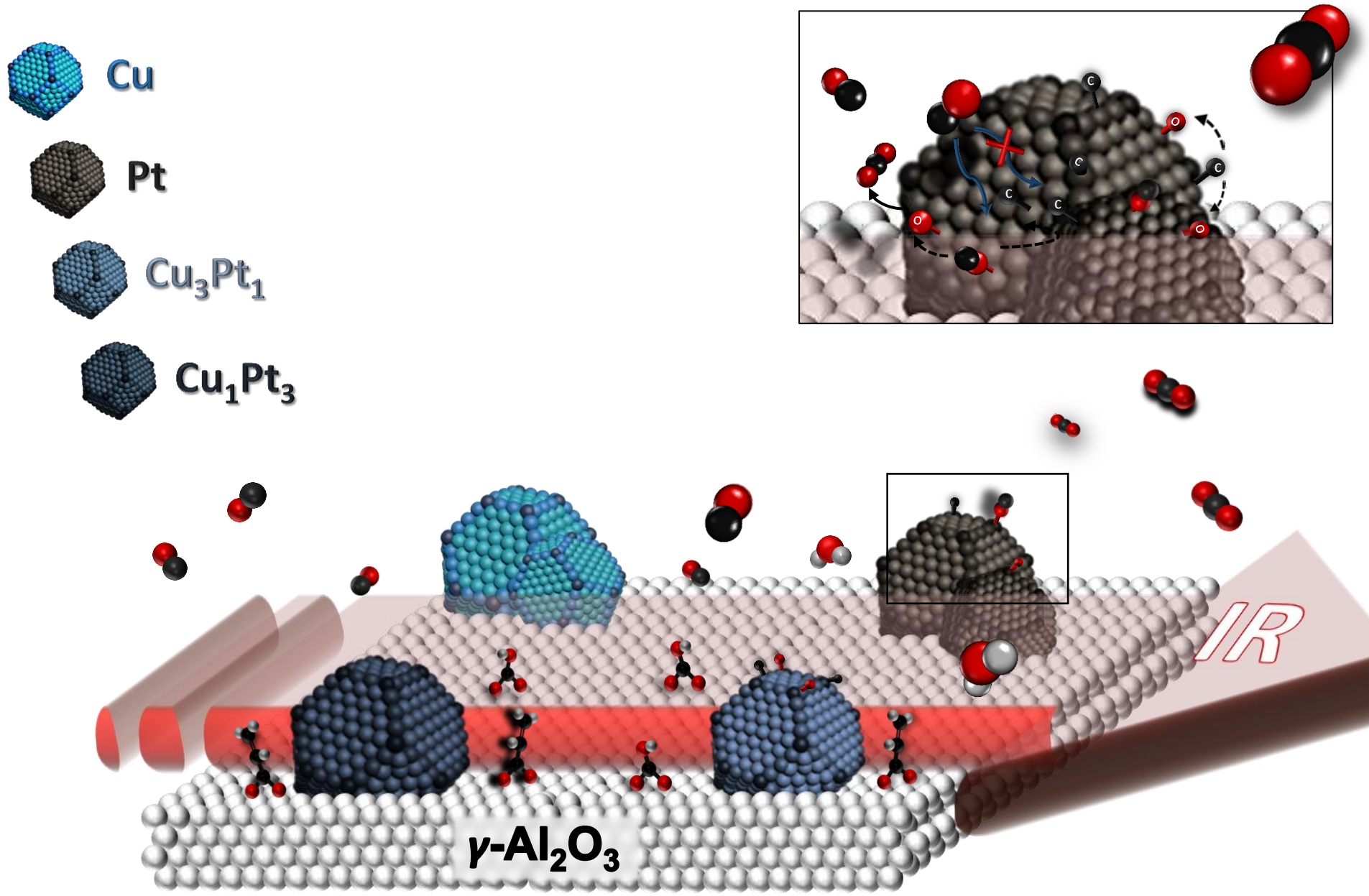
Cu
Pt
Cu_3Pt_1
Cu_1Pt_3
C
O
IR
γ-Al_2O_3